Electrodeposition of nanostructured cobalt films from a deep eutectic solvent: Influence of the substrate and deposition potential range

Midori Landa-Castro[1,2], Paula Sebastián[2,3*],Marina. I. Giannotti[2,4,5], Albert Serrà[6], Elvira Gómez[2,7]

[1] Universidad Autónoma Metropolitana-Azcapotzalco, Departamento de Materiales, Av. San Pablo 180 Col, México

[2] Departament de Ciència de Materials i Química Física, Universitat de Barcelona, Martí i Franquès, 1, 08028 Barcelona, Spain.

[3] Department of Chemistry, University of Copenhagen, Universitetsparken 5, 2100 Copenhagen, Denmark

[4] Biomedical Research Networking Center on Bioengineering, Biomaterials and Nanomedicine (CIBER-BBN), Spain.

[5] Institut de Bioenginyeria de Catalunya (IBEC), The Barcelona Institute of Science and Technology, Barcelona, Spain.

[6] Empa, Swiss Federal Laboratories for Materials Science and Technology, Laboratory for Mechanics of Materials and Nanostructures, Feuerwerkerstrasse 39, CH-3602 Thun, Switzerland.

[7] Institute of Nanoscience and Nanotechnology (IN^{2}UB), Universitat de Barcelona, Barcelona, Spain.

*Corresponding author: paula.sebastian25@gmail.com

Abstract

The purpose of this systematic study was to investigate the effects of specific substrates and potential conditions applied while tailoring the morphology and chemical composition of nanostructured Co films. In particular, Co electrodeposition in sustainable choline chloride-urea deep eutectic solvent was assessed, using glassy carbon and two metals widely employed in electrocatalysis and biocompatible purposes, Pt and Au, as substrates for modification with Co. Various in situ electrochemical techniques were combined with a broad range of ex-situ characterization and chemical-composition techniques for a detailed analysis of the prepared Co films. Among the results, nanostructured Co films with high extended active surface areas and variable composition of oxo and hydroxyl species could be tuned by simply modulating the applied potential limits, and without using additives or surfactant agents. The study highlights the effectiveness of using deep eutectic solvent as suitable electrolyte for surface modification by controlled deposition of nanostructured Co films with further application in electrocatalysis.

Keywords: cobalt electrodeposition, deep eutectic solvent, first growth stages, substrate influence.

Graphical abstract

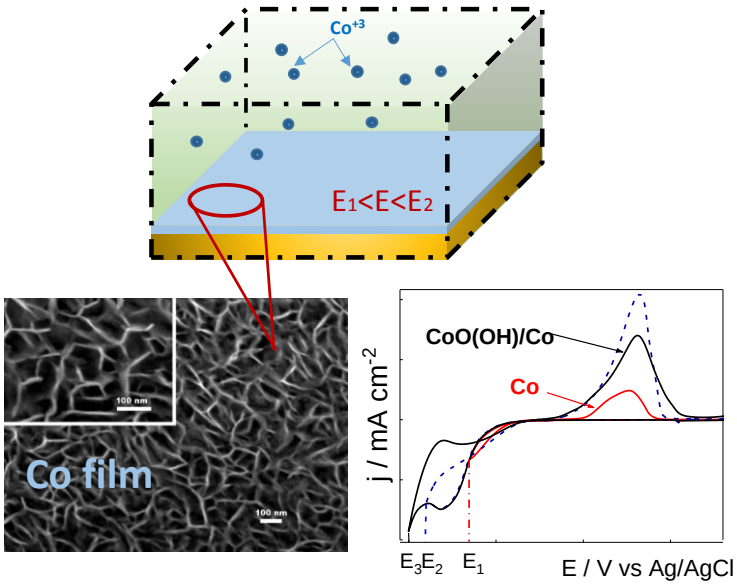

1. Introduction

With extensive technological developments worldwide, there is an urgent demand for materials with suitable characteristics in energy conversion, water remediation, CO_2 reduction, electronics manufacturers, and various other industries. This is particularly important for the transition from traditional energy generation to a decarbonized economy and clean energy scheme.[1,2] To overcome the challenges of this conversion, the scientific community has been investing considerable efforts to develop energy efficient processes and explore environmentally-friendly strategies without compromising competitiveness. In real applications, efficient processes require powerful electrocatalysts that lower the energy to drive reaction at competitive rates. To address these challenges, electrochemistry has proven to play a crucial role. Electrochemistry deals with the conversion of energy stored in chemical bonds intro electricity and vice versa. Electrochemistry involves the storage of energy (e.g., batteries) [3,4], transformation of fuels (e.g., ethanol, methanol) [5,6], electrolysis (e.g., hydrogen) [7,8], and synthesis of materials via electrodeposition [9,10].

Electrodeposition is a versatile tool to prepare various materials, such as metallic films, metal oxides, composites [11,12], and micro-nanostructured materials [13]. Among other benefits, electrodeposition is cheaper in terms of equipment than some available deposition techniques. This appealing technique also allows tuning of the properties of the final deposit by simply modifying the deposition conditions, such as the reactant or electrolyte source, concentration, solution pH, additives, and electrochemical parameters, including applied potential/current, charge, deposition time, and signal type [14]. Another key parameter to consider is the incorporation of foreign species into the solution that may interfere with the deposition process [15]. Since the electrodeposition process largely depends on the material of the electrode [16], detailed knowledge of the effects of different parameters on the deposition process is crucial for developing the material on a rational basis. Therefore, electrodeposition serves as a powerful tool for material preparation in the emerging energy conservation industry.

Traditionally, electrodeposition has been carried out in aqueous electrolytes. However, aqueous media have a narrow electrochemical window, limiting the deposition of metals with very negative reduction potentials, and interfering with highly electrocatalytic metals due to the hydrogen evolution reaction [17,18]. Consequently, the

electrodeposition of such metals overlaps with solvent reduction, which promotes hydrogen reaction as well as the consequent local pH increase near the growing deposit [19]. This occurrence is caused by the consumption of protons or formation of hydroxide ions, decreasing current efficiencies and even modifying the final deposition process.

Aiming to facilitate the deposition of some metals, ionic liquids (ILs) have emerged as alternative solvents in the past decades because they offer wide electrochemical potential window [20]. However, their use has been restricted due to mandatory careful handling [21], high costs, and emerging studies of their harmful effects in humans [22]. Towards the development of environmentally friendly methods, a new class of non-toxic and inexpensive ionic liquids, known as deep eutectic solvents (DESs), are being used to conduct electrodeposition of metals and alloys [23–27]. DESs, introduced by Abbott and co-workers [28], are eutectic mixtures of a quaternary ammonium halide with a hydrogen-bond donor. They demonstrated unusually high solubility for metal salts, metal oxides and hydroxides, in addition to low water sensitivity [29]. Their high viscosity and low transport properties facilitate deposition control, a factor that could be highly relevant in the design of new electrocatalysts [30]. It is worth noting that, in the study of reduction processes in DESs, the effects of the presence of water and the hydrogen donor characteristic of DES component [31] during reduction processes has rarely been considered, and even less so their effects on the final deposit. The increase in water content in the DES reduces its electrochemical stability with a subsequent shortening of the electrochemical window, accentuated when highly electrocatalytic substrates are used [32,33].

Among other metals, cobalt and cobalt alloys are widely used in both catalytic [34] and magnetic applications [35] due to their outstanding properties. The electrodeposition of cobalt in different aqueous electrolytes has been widely studied [36,37], but the preparation of the cobalt deposit usually requires strict control of the electrodeposition parameters, and hydrogen co-reduction appears easily. Cobalt deposition in DESs was previously studied under restricted conditions at low overpotentials over vitreous carbon and copper electrodes [38–41], establishing that, on these substrates, cobalt deposition proceeds via nucleation and 3D growth processes.

This work aims at an in-depth study of cobalt electrodeposition behavior in DESs using three different substrates. As knowledge about a given subject is generally acquired in a stepwise manner, allowing information gained by solving the simplest cases to then be

transferred to more complicated cases, glassy carbon was the first electrode selected due to its high polarizability. Following this, two noble metals, platinum and gold were used. These two metals are used in catalytic and biocompatible processes, making them suitable surfaces to be decorated with cobalt for different applications. The cobalt deposition process was analyzed under a wide potential range, in order to investigate whether different cobalt species are formed depending on the nature of the substrate and the potential range. Interest was also focused on evaluating the influence of possible DES reduction coupled with cobalt electrodeposition and whether this affects the distribution, nature and structure of the deposited cobalt species on each one of the selected substrates. Electrochemical behavior was analyzed by means of cyclic voltammetry, voltammetric-potential hold, chrono-amperometric and galvanostatic techniques. Specific electrochemical behavior associated with the first stages on noble electrodes was also investigated. The morphology of the cobalt deposits was characterized using field emission scanning electron microscopy (FE-SEM). Atomic force microscopy (AFM) was employed to analyze a Pt(111) surface modified by low amounts of cobalt in order to assess the process on the initial steps of cobalt electrodeposition. Compositional analysis by means of electron dispersive microscopy and X-ray photoelectron spectroscopy (EDS and XPS, respectively) was also carried out. Structural characterization from X-ray diffraction measurements (XRD) was made for the deposits obtained.

2. Experimental

The DES was prepared using analytical-grade choline chloride (ChCl, Across Organics) and urea (Merck). ChCl was dried in an oven at 70 °C for 48 h and placed in a desiccator, after which the DES was prepared by mixing amounts of ChCl and urea in a 1:2 molar ratio at approximately 50 ^{o}C until becoming liquid. The liquid was dried under vacuum, stirring, and heating conditions (T < 50 ^{o}C) overnight. To prepare the cobalt bath, 99% pure $CoCl_2{*}6H_2O$ salt (Merck) was dried at 100 ^{o}C for 10 h until dehydrated and added to the DES. To dissolve the cobalt salt in the DES, the mixture was stirred and subsequently kept under vacuum and heating (40-50 $^{\circ}$C) conditions for 24 h. [18,32,42] The water content in the DES was estimated as around 1 % according to the blank cyclic voltammograms recorded on a Pt electrode after adding different percentages of water, following the procedure reported in a previous publication.[32]

Five working electrodes were used: a glassy carbon (GC) rod (0.0314 cm^2), a Pt polyoriented bead electrode (0.22 cm^2), a Pt(111) single crystal (0.048 cm^2) cut from a single crystal bead following Clavilier's method,[43] an Au(poly) bead (0.15 cm^2), and flat silicon pieces with a seed layer containing Ti(15nm) and Au(100nm), hereafter called "Si/Ti/Au". Specific pre-treatments were used for each of the surfaces. The glassy carbon electrode was polished to a mirror finish with alumina of different grades (3.75 and 1.87 μm; VWR Prolabo), cleaned ultrasonically for 2 min in water treated with the Milli Q system (Millipore), and dried with argon prior to immersion in the solution. By contrast, the Au bead was flame annealed to remove organic contaminants from the surface, whereas Pt(poly) and Pt(111) were cleaned by flame annealing followed by cooling in an argon atmosphere in the electrochemical cell to prevent the oxygen reaction on the surface. Last, the pieces of Si/Ti/Au were cleaned with ethanol and acetone. Once cooled, all electrodes were immersed in the DES. In the case of Pt(111), a meniscus configuration was employed.

To perform the electrochemical experiments, a thermostated cell with a three-electrode configuration was employed. The reference electrode was Ag|AgCl|Cl^- mounted in a Lugging capillary containing the DES, whereas the counter electrode was a platinum spiral. Throughout the experiments, the temperature was kept at 70 ºC.

Electrochemical measurements were carried out using a potentiostat (PGSTAT 12, Autolab). The morphology of the samples was analyzed using a field emission scanning electron microscope (FE-SEM; JSM-7100F Analytical Microscopy). X-ray diffraction (XRD) patterns were recorded using a diffractometer (PANalytical X'Pert-PRO MRD) with parallel optical geometry in a grazing incidence configuration (1º) with Cu K_α radiation (λ = 0.1542 nm). A 2θ scan, between 20 and 100º, was used, with a step size of 0.05 and a measuring time of 15 s per step. All spectra were collected using Al K_α radiation (1,486.6 eV). X-ray photoelectron spectroscopy (XPS) measurements were taken with an XPS system (PHI 5600 Multitechnique, Physical Electronics) using a monochromatic X-ray source (Al K_α line = 1,486.6 eV, 350 W). The area analyzed was a circle 0.8 mm in diameter, and all measurements were made in an ultra-high vacuum chamber. Cobalt deposits were etched by means of argon ion sputtering up to a few nanometers prior to acquiring angle-resolved (AR) XPS images. Multipak 8.2 was used to acquire digital images and to perform peak deconvolution, while atomic force microscopy (AFM) images were obtained with an AFM (Asylum Research MFP-3D,

Oxford Instruments) using V-shaped Si_3N_4 cantilevers with sharp silicon tips, and nominal spring constant in the range 0.06-0.24 N m^{-1} (SNL, Bruker AFM Probes). Images were acquired in contact mode at room temperature in a liquid environment (Ultra-pure Water System, MilliQ) and processed with the AR software. Prior to characterization, the samples were exhaustively cleaned under warm water for the time needed to entirely remove the DES residues.

3. Results

3.1. Cobalt deposition

3.1.1. Glassy carbon electrode

Before studying the cobalt electrodeposition, the electrochemical window in the DES blank solution for each of the substrates was analyzed at 70 ºC and at scan rate of 50 mV s^{-1} (Figure S1). Using glassy carbon as the substrate, an electrochemical window wider than 3 V was recorded. The electrochemical window was dramatically shortened on the bare Pt electrode, especially in the negative potential zone. Remarkably, reversing the scan after the primary reduction process caused the positive scan to show a prominent oxidation peak at approximately -1.2 V. That voltammetric feature increased in current density by enlarging the negative limit, thereby indicating that its origin was linked to the solvent's reduction. However, the peak disappeared when cyclic voltammetry (CV) was performed under stirring conditions, which was previously attributed to the formation of hydrogen gas on Pt from the solvent's reduction [33]. In the experiments, the formation of gas bubbles on the electrode's surface as a reduction product was observed after sufficiently elongating the negative scan. Using Au electrodes, an intermediate electrochemical window between GC and Pt was recorded. However, Au was more active than GC and Pt in relation to the oxidation of the DES and displayed a broad band, which origin is unclear, at the onset of the solvent's massive oxidation. [44]

Cobalt deposition on glassy carbon and in DES was at first assessed. Figure 1 shows the cyclic voltammograms of the deposition of cobalt on vitreous carbon. In general, the results obtained at moderate potential limits align with previously reported findings [38,39] (Figure 1A). A typical nucleation loop was recorded in the positive scan (Figure 1A, curve a, indicated by arrows), followed by an oxidation peak, peak A_1. Elongating

the negative scan revealed that a clear reduction peak, peak C_1 (Figure 1A, curve b) had developed and that the oxidation peak A_1 had increased in intensity and charge. The reduction peak C_1 was followed by the reduction of the DES, a process clearly activated by depositing cobalt on the vitreous carbon substrate, which decreased the overpotential needed to reduce the DES (Figure 1B, curve a). Scanning toward the potentials overlapping the massive DES reduction, revealed a dramatic diminution of the oxidation charge under peak A_1, and that diminution was even more evident as the cathodic voltammetric limit became increasingly negative (Figure 1B, curve b). Furthermore, a current band centered around 1 V was recorded, followed by a new feature previous to massive solvent oxidation (Figure 1B, curve b). Such results suggest that reducing the DES during the deposition of cobalt induced the surface passivation of the cobalt deposit [18,32,45].

To further examine the effect of the co-reduction of the DES solvent with the deposition of cobalt, voltammetric holds at different potential values were performed. Figure 1C presents a comparison of the CV of the deposition at 50 mV s^{-1} with the same CV after holding the potential at -1.2 V for 30 s. As expected, the oxidation charge under the A_1 peak increased due to having the highest amount of deposited metallic cobalt. No splitting in the oxidation peak or in new peaks in the anodic scan was observed, which supports the idea that only a single-phase cobalt deposit was obtained in these conditions. However, holding the potential at values more negative than those corresponding to the C_1 peak in Figure 1D caused considerable changes in the voltammetric profile shown in the positive scan. A clear diminution of the charge involved under the A_1 peak was observed, followed by an oxidation band that preceded an important current increase from 0.6 V (Figure 1D).

Those voltammetric results suggest that the solvent did react on the freshly deposited cobalt. When the threshold potential value was attained, the reduction of the DES caused the formation of species that hindered the deposit's oxidation. As evidence the Q_{ox}/Q_{red} ratio exceeded 95% when overpotentials were moderate, despite dropping significantly after the overpotentials were sufficiently increased (Table 1).

<Table 1>

<Figure 1>

The potentiostatic experiments performed at low overpotentials corroborated the voltammetric results. The recorded j-t transients displayed a profile indicating that the deposition of cobalt was controlled by a mechanism of nucleation and 3D growth (Figure 2A). The overlapping of the currents, at deposition times exceeding the corresponding t_m, confirms mass control during cobalt's deposition in the DES and the absence of hydrogen reaction in that range of potential. Herein, t_m is the time at which the maximum current value is attained at the curve (j_m-t_m), from which the deposition process follows linear diffusion control. Galvanostatic experiments under moderate current demand revealed the typical spike in nucleation, meaning that the potential initially dropped to a value at which sufficient nuclei were formed before subsequently reaching a quasi-stationary value (Figure 2B). The potential spike appeared at more negative potentials and at low deposition times as the fixed current density increased. Afterward, the potential became increasingly negative until plateauing at longer times, thereby demonstrating the effect of mass control.

<Figure 2>

The morphology of different samples of cobalt deposits, prepared under different conditions, was assessed by FE-SEM. Deposits were prepared by potentiostatically selecting the applied potential according to the voltammetric results. Figure 3 shows the cobalt deposits prepared on vitreous carbon at two potentials and at a moderate deposition charge. The deposit obtained at the low overpotential displayed grains that did not coalesce and with shape similar to a desert rose (Figure 3A and 3B), meaning that the grains resulted from the agglomeration of emerging spines. After increasing the overpotential applied the deposit showed a similar open morphology but with smoother edges (Figure 3C). In both cases, the grains formed a network structure with a highly exposed active area. Due to the possibility of a solvent reaction, deposits were prepared under moderate potentials at which passivation was irrelevant. A qualitative compositional analysis of some prepared deposits using energy-dispersive X-ray spectroscopy (EDS) revealed that cobalt is the main species of the prepared deposits at

the lowest overpotentials, but as overpotential increase, oxygen is detected to rise (Figure S2)

<Figure 3>

3.1.2. Platinum electrode

Figure 4 shows the CV of the cobalt deposition on polycrystalline Pt (Pt(poly)). For comparison, the curves of cobalt's deposition were plotted with the blank cyclic voltammogram of the DES on Pt. The electrodeposition of cobalt initiated closely to, if not at more advanced degree than, previous reduction processes observed in the blank solution (Figure 4A). When the negative scan was performed at low negative potential values, a nucleation loop did not appear in the reverse scan. Nevertheless, deposition occurred, confirmed by the Co oxidation peak in the positive scan (Figure 4A, curve a). Interestingly, by enlarging the negative scan to lower values (Figure 4A, curve b), a small activation of Co deposition was observed in the reverse scan. This behavior suggested that Co deposition on Pt begins with the deposition of a Co adlayer or submonolayer subsequently proceeding via nucleation and growth. Figure 4B illustrates that the massive deposition of cobalt developed a clear reduction peak (Figure 4B, curves a and c), while the appearance of the solvent's massive reduction was delayed at more negative potentials than those on bare Pt (Figure 4B, curve c). Such results highlight that platinum's surface decorated with cobalt was less active than bare Pt (Figure 4B, curve b) in relation to the solvent's reduction.[32,46] Increasing the negative voltammetric limit caused the oxidation charge in the reverse scan to gradually decrease, especially after potential limits overlapping the solvent's massive reduction were reached.

Potentiostatic experiments on Pt confirm that the deposition of cobalt on the substrate overlapped in some processes related to the presence of DES. The j-t transients showed a current exceeding the capacitive one at low deposition times; that current, related to the solvent reaction, overlapped with the corresponding current of the deposition of cobalt (Figure 4C). The recorded j-t transients also revealed a typical nucleation maximum and smooth current decay, albeit no overlap between the curves queues, suggesting that an additional simultaneous process occurred. In galvanostatic experiments the currents were selected in terms of previous voltammetric characterization, the E-t curves recorded under low current demand showed profiles without features of nucleation (Figure 4D). The characteristic nucleation spike appeared only in the curves recorded when a certain

threshold current value was applied. Extending the deposition caused the expected potential-time profile for mass-controlled nucleation and growth to appear

<Figure 4>

The FE-SEM analysis showed that deposits prepared using Pt as the substrate consisted of thin platelets with a reticular structure and randomly distributed smooth edges, oriented vertically to the surface, thereby appearing to be interwoven (Figure 5A). A reasonable explanation for the origin of such smoothness in the morphology is that the reaction of the DES affects the deposition on Pt but not on glassy carbon. The deposits obtained by increasing the overpotential did not show relevant morphological changes; the interwoven morphology was obtained, albeit with ridges neither as sharp nor as thick (Figure 5B). Remarkably, similar morphology was also observed for the cobalt electrodeposits in ethylene glycol deep eutectic solvent on Cu electrode, a catalyst that is also highly active for several electrocatalytic reactions.[47–49] Even for deposits prepared at the lowest overpotentials, the EDS analysis revealed the presence of oxygen, possibly related to the catalytic DES reaction of the substrate (Figure S3).

<Figure 5>

To investigate the singular electrochemical response obtained during the initial stages of cobalt's reduction on platinum, the morphological aspect of cobalt's deposition on platinum in low amounts of coverage was assessed after low reduction charges were applied. Different samples were prepared in the range of potential in which features typically related to the nucleation are absent. AFM characterization of a modified well-ordered monocrystalline platinum substrate Pt(111) with cobalt was carried out. Given its flat surface, Pt(111) was selected as a model for the AFM analysis to avoid defects and irregularities in the polycrystalline substrate from complicating analysis during the first stage of deposition, which are particularly sensitive to surface ordering. Figure 6A shows the AFM images of Pt(111) modified by cobalt obtained by applying lower overpotential values, a pseudo-platelet structure can be observed in which the flat structures are homogeneously distributed along the substrate. When the charge was increased, 3D growth was not observed in that range of potential. Such results agree with the lack of nucleation features in the electrochemical curves recorded under the same conditions.
The observed morphology is compatible with 2D growth, which supports the idea that 2D growth could occur before the growth of the 3D deposit (i.e., deposition via the

Stranski−Krastanov mechanism) [32]. As a possible explanation, such results could be associated with the high amount of chloride in the DES, aside from the rest of the species, all of which adsorb and strongly interact with both the cobalt and the Pt(111) substrate. Thus, they could act as surfactant agents that hinder the 3D growth of cobalt at sufficiently low potentials.

Samples prepared at more negative overpotentials clearly revealed the formation of cobalt nanoparticles similarly sized to those formed on the Pt(111) substrate (Figure 6B). That outcomes suggests that, in that range of overpotential, instantaneous nucleation governs the first stages of mechanism of deposition on platinum. By slightly increasing the overpotential and the charge involved, the formation of incipient needles was imaged (Figure 6C) as a consequence of the collapsed growth of first formed grains. Such structures seem to be precursors of the characteristic final morphology of cobalt deposits, reminiscent of desert roses.

<Figure 6>

3.1.3. Gold electrode

Given the interest in the cobalt's functionalization of different substrates that could act as electrocatalysts or materials for different processes, we also investigated the deposition of cobalt on different gold substrates. The bulk deposition of cobalt began at -0.9 V, and during the voltammetric scan, a clear reduction peak (C_1) developed before the solvent's massive reduction (Figure 7A). Shown in the positive scan, a single oxidation peak (A_1) developed. Reversing the scan at potential values exceeding the peak, the recorded oxidation charge under peak A_1 diminished and the initiation of the massive oxidation current was delayed until more positive values arose. Corresponding to nucleation and growth, reversing the scan at the outset of deposition caused the typical nucleation loop to appear. Similar to what occurred with vitreous carbon, the massive reduction in the solvent's current was activated on the gold modified by cobalt, likely due to the higher electrocatalytic activity of cobalt than gold in relation to the solvent's reduction. By contrast, the Co-Au modified surface enlarged the oxidation potential limit compared with pure gold. Similar behavior was recorded on the Si/Ti/Au substrate (Figure S4). Shortening the cathodic scan up to -0.8 V, two small irreversible peaks were observed prior to the bulk deposition (Figure 7A, inset, black curve), preceded by a voltammetric nucleation loop (Figure 7A, red curve). This could relate to underpotential deposition (UPD) of a layer of cobalt on gold. After all, the UPD of copper and silver on gold in a

DES has previously been described, which suggested the possibility that the formation of chloride complexes greatly enhances the UPD in the DES [44,50–52].

The j-t transients at different applied potentials for the deposition of cobalt on gold were recorded. The curves revealed the characteristic nucleation maximum, and at longer times, the current curve overlapped, thereby corresponding to a mass-controlled process (Figure S5, A). Remarkably, capacitive current exceeded that observed on vitreous carbon, which showcases the sensitiveness of deposition to the nature of the substrate. Processes prior to nucleation and growth were also revealed in the galvanostatic curves (Figure S5, B). At sufficiently low applied current densities, processes that could correspond to the UPD, solvent adsorption, or reaction on Au occurred. By increasing the applied current, the typical current spikes appeared and the potential shifted to more negative values as the current demanded rose. By sufficiently increasing demanded current or time deposition, the attained potential corresponded to the solvent's massive reduction, as occurred on all analyzed substrates.

The prepared deposits showed an interwoven morphology similar to that obtained on platinum, one with thin platelets randomly distributed and vertically oriented, albeit with sharper edges than those obtained on Pt (Figure 7B and 7C). Increasing the applied overpotential did not promote relevant morphological changes. Such results suggest that the morphology is preferred when cobalt is deposited on metallic surfaces, in which its interaction with another metal is stronger than with vitreous carbon, thereby inducing the particular interwoven appearance. Conversely, the EDS showed that on Au surfaces, including the sputtered Au substrate, Co deposition could occur without interference from other reactions. Oxygen was detected by raising the overpotential. (Figure S6).

<Figure 7>

The different voltammetric behaviors reordered in the oxidation sweep at different potential limits together with the progressive increase in oxygen content by increasing the cathodic potential limit has helped attain detailed structural and compositional characterization of the deposits. For comparison, the analyzed deposits were also prepared on Si/Ti/Au substrates at both low and high applied overpotentials.

Similar to what occurred while using Pt as a substrate, despite no relevant changes in the morphology of the deposits when the applied overpotential was increased, the crystal structures clearly differed (Figure 8). All of the diffraction patterns presented three intense

peaks corresponding to the Si/Ti/Au substrate: reflections (111) and (222) of Au and (004) of Si. However, the magnified pattern allowed characterizing the crystal structural characteristics of each deposit. At -0.96 V (Figure 8, curve ii), the XRD patterns confirmed the electrodeposition of metallic cobalt, with seven diffraction peaks at 2θ values of 41.7°, 44.6°, 47.6°, 73.9°, 92.6°, 94.7°, and 98.7°. All of those peaks perfectly matched with the (100), (002), (101), (110), (112), (201), and (004) plane reflections of the hcp cobalt phase (ICCD 00-005-0727). At the same time, all of the diffraction peaks were relatively wide, being more significant at large angles, thereby suggesting shape anisotropy [53,54]. The high relative intensity of the 2θ 44.8° peak indicated a clear (002)-preferred orientation. When cobalt's electrodeposition was performed with higher applied overpotentials (Figure 8, curve iii)—at which the DES was clearly reduced—six diffraction peaks at 2θ values of 32.5°, 51.4°, 57.9°, 61.6°, 69.6°, and 71.4° were observed. All of those peaks matched perfectly with the (100), (012), (110), (111), (103), and (021) plane reflections of hexagonal $Co(OH)_2$ (ICCD 01-074-1057). Moreover, all of the peaks were wide and more accentuated at high 2θ values, which may indicate shape anisotropy [53,54]. The reduction of the DES clearly affected the deposition of cobalt, suggesting greater relevant in the electroprecipitation of $Co(OH)_2$ than in the reduction of Co(II). The dashed lines in the graphs indicate the peaks of the standards.

<Figure 8>

To further investigate the chemical composition and chemical states of the elements of the prepared deposits, by XPS analyses were conducted. All of the XPS spectra were corrected relative to the binding energy of C 1s peak (284.6 eV). The complex spectrum of Co 2p, characterized by two components—Co $2p_{3/2}$ and Co $2p_{1/2}$—due to spin-orbital splitting and the shake-up satellites, provide important information about its chemical states [55–57]. As shown in Figure 9A, the deposits prepared at -0.96 V were mainly metallic cobalt, given that an asymmetric main peak at approximately 778.1 eV with two plasmon-loss peaks corresponding to Co $2p_{3/2}$ and another peak at approximately 793.2 eV corresponding to Co $2p_{1/2}$ were detected. However, the asymmetric peak at 793.2 eV and the impossibility of deconvoluting the two plasmon-loss peaks corresponding to Co $2p_{3/2}$ at 3.0 and 5.0 eV above the primary peak (approx. -778.1 eV) also revealed the presence of Co^{2+}, possibly $Co(OH)_2$ [58,59]. Importantly, the electrodeposited Co(II) species at -0.96 V were amorphous, as evidenced by the lack of any features in the XRD

pattern (Figure 8, curve ii). However, the weakness of those signals also indicates that the majority of the cobalt existed in the form of Co(0).”

However, the weakness of those signals also indicates that the majority of the cobalt existed in the form of Co(0). The spin-orbit coupling of 15.1 eV (i.e., the difference in binding energy between the Co $2p_{3/2}$ and Co $2p_{1/2}$ peaks) was also consistent with metallic cobalt, because higher values are expected for Co(II) and Co(III) species. The O 1s spectra of the sample show a predominant contribution of oxygen at a binding energy of approximately 530.2 eV, which is assigned to metal oxide bonds and the presence of oxygen in hydroxide groups, and a smaller shoulder at approximately 531.4 eV (possibly structural water) [55–59]. However, the oxygen peak was barely visible, especially after various sputter cycles, when compared with the cobalt ones. The Co/O atomic ratio was approximately 19, which confirmed the deposition of metallic cobalt at these conditions. By contrast, the Co 2p spectrum of the deposits prepared at the higher overpotentials, at -1.35 V (Figure 9B) showed contributions of cobalt’s peaks at binding energies of approximately 780.1 and 795.9 eV, thereby corresponding to Co $2p_{3/2}$ and Co $2p_{1/2}$, respectively, and non-depreciable satellite peaks at approximately 785.5 and 802.1 eV, all ascribed to Co^{2+}. The O 1s spectra of the sample additionally showed two predominant contributions of oxygen at binding energies of approximately 528.4 and 530.2 eV, both attributed to CoO and $Co(OH)_2$, and a smaller shoulder at approximately 531.4 eV (possibly structural water) [55–59]. The XPS spectra were practically visible during various sputter cycles, which indicates the excellent homogeneity of the deposited cobalt. All of those findings are consistent with the results of the EDS analyses.

<Figure 9>

4. Conclusions

The present work aimed to analyze Co electrodeposition in the choline chloride-urea DES. Herein, the influence of both the nature of the substrate and selected potential range on the morphology and chemical composition of cobalt deposits was investigated. Different electrochemical and surface *ex-situ* characterization techniques were combined to provide detailed descriptions of the parameters controlling deposition.

Cyclic voltammetry with potentiostatic and galvanostatic measurements were used to analyze the reduction of Co in DES. The potential control and galvanostatic experiments confirmed that Co deposition in DES proceeds through nucleation and 3D growth mechanisms. On amorphous vitreous carbon, nucleation occurs on the substrate once the necessary energy input is attained. Contrarily, on metallic substrates, such as Au and Pt, tentative underpotential deposition or adlayer deposition of Co possibly occurs before the subsequent nucleation and growth of the Co structure. Voltammetric results revealed that the typical nucleation current loop does not appear on Pt and Au substrates, unless a threshold potential value is reached. This behavior is also consistent with the galvanostatic experiments performed at very low currents, in which a nucleation spike was not recorded. The recorded potentiostatic curves demonstrated that currents related to nucleation and growth processes overlapped with a different process, possibly related to adlayer Co formation.

To gain deeper insight into the Co deposition on metallic substrates, a single crystalline Pt electrode was selected as a model surface to investigate the first stages of Co deposition. The corresponding AFM images obtained on the well-ordered platinum, applying very low overpotentials, corroborated the formation of a 2D deposit at low applied charges. However, slightly increasing the overpotential and flowing charge resulted in nanoparticle formation that developed needles along the substrate, which are reminiscent of Co deposits' characteristic morphology. The conditions under which the nanoparticles were imaged in AFM aligned with the nucleation features observed in the electrochemical analysis. The morphology of the final deposit imaged by FE-SEM on both Au and Pt, differs from that obtained on vitreous carbon. On vitreous carbon desert roses, morphology and formation of grains were imaged, likely induced by high surface diffusion on this substrate. In contrast, deposits obtained at low and moderate overpotentials on Au and Pt displayed an open interwoven morphology. The deposits on Pt showed a certain oxygen content even at low applied overpotentials, likely due to the high activity of substrate towards the reduction of the DES and water traces.

The electrochemical analysis of the deposition process at high overpotentials showed that passivation processes related to solvent reaction occurred, demonstrated by a drastic decrease in the Q_{ox}/Q_{red} ratio with the enlarging voltammetric negative limit. Deposited Co activated the massive solvent reduction process more than the bare glassy carbon or gold substrates. The co-reduction of Co and DES was responsible for the formation of

hydroxylated Co species. On the Pt electrode, only fewer negative overpotentials were needed to detect the presence of hydroxylated Co species, possibly due to the highest catalytic activity of Pt during DES reduction. Different hydroxo species were confirmed after the morphological, structural, and compositional characterization of the final deposits. This formation might be related to the increased local pH level caused by either the reaction of the hydrogen donor character of urea in the eutectic solvent or low water content of the solution.

This evidence reported corroborates that substrates with different electrocatalytic properties can be decorated with nanostructured Co, by conveniently tailoring the electrodeposition conditions in DES. Remarkably, oxidized cobalt species can be prepared, both being useful in different applications, particularly for electrocatalytic studies in alkaline media. Moreover, the deposits obtained on metallic substrates exhibited an open structure, resulting in high effective surface area, which ultimately causes enhanced electrochemical reactivity and increases its ability to be functionalized.

Acknowledgements

This work was supported by the TEC2017-85059-C3-2-R projects (financed by the *Fondo Europeo de Desarrollo Regional*, FEDER) from the Spanish *Ministerio de Economía y Competitividad* (MINECO). MIG acknowledges 2017-SGR-1442 project from Generalitat de Catalunya and MLC thanks CONACyT for the studentship given to pursue her M. Sc & Eng. posgraduate studies and a research stay at Universitat de Barcelona. The authors also thank the CCiT-UB for the use of their equipment and Prof. Juan Feliu from university of Alicante to provide us Pt(111) substrate.

Appendix A. Supplementary data

Supplementary data related to this article can be found, in the online version, at doi:

References

[1] S. Chu, Y. Cui, N. Liu, The path towards sustainable energy, Nat. Mater. 16 (2016) 16–22. https://doi.org/10.1038/nmat4834.

[2] R. Eisenberg, H.B. Gray, G.W. Crabtree, Addressing the challenge of carbon-free energy., Proc. Natl. Acad. Sci. U. S. A. (2019) 201821674.

https://doi.org/10.1073/pnas.1821674116.

[3] N. Nitta, F. Wu, J.T. Lee, G. Yushin, Li-ion battery materials: Present and future, Mater. Today. 18 (2015) 252–264. https://doi.org/10.1016/j.mattod.2014.10.040.

[4] T. Kim, W. Song, D.Y. Son, L.K. Ono, Y. Qi, Lithium-ion batteries: outlook on present, future, and hybridized technologies, J. Mater. Chem. A. 7 (2019) 2942–2964. https://doi.org/10.1039/C8TA10513H.

[5] D. Hart, F. Lehner, S. Jones, J. Lewis, The Fuel Cell Industry Review 2019, (2019) 1–52. www.FuelCellIndustryReview.com.

[6] D.R. Dekel, Review of cell performance in anion exchange membrane fuel cells, J. Power Sources. 375 (2018) 158–169. https://doi.org/10.1016/j.jpowsour.2017.07.117.

[7] S. Shiva Kumar, V. Himabindu, Hydrogen production by PEM water electrolysis – A review, Mater. Sci. Energy Technol. 2 (2019) 442–454. https://doi.org/10.1016/j.mset.2019.03.002.

[8] Z. Yan, J.L. Hitt, J.A. Turner, T.E. Mallouk, Renewable electricity storage using electrolysis, Proc. Natl. Acad. Sci. 2019 (2019) 201821686. https://doi.org/10.1073/pnas.1821686116.

[9] G.R. Li, H. Xu, X.F. Lu, J.X. Feng, Y.X. Tong, C.Y. Su, Electrochemical synthesis of nanostructured materials for electrochemical energy conversion and storage, Nanoscale. 5 (2013) 4056–4069. https://doi.org/10.1039/c3nr00607g.

[10] A. Serrà, E. Vallés, Advanced electrochemical synthesis of multicomponent metallic nanorods and nanowires: Fundamentals and applications, Appl. Mater. Today. 12 (2018) 207–234. https://doi.org/10.1016/j.apmt.2018.05.006.

[11] N.F. Heinig, N. Kharbanda, M.R. Pynenburg, X.J. Zhou, G.A. Schultz, K.T. Leung, The growth of nickel nanoparticles on conductive polymer composite electrodes, Mater. Lett. 62 (2008) 2285–2288. https://doi.org/10.1016/j.matlet.2007.11.094.

[12] E. Gómez, S. Pané, E. Vallés, Magnetic composites CoNi-barium ferrite prepared by electrodeposition, Electrochem. Commun. 7 (2005) 1225–1231. https://doi.org/10.1016/j.elecom.2005.08.016.

[13] F. Nasirpouri, Electrodeposition of Nanostructured Materials, 49 (2017) 1–325. https://doi.org/10.1007/978-3-319-44920-3.

[14] D. Thiemig, R. Lange, A. Bund, Influence of pulse plating parameters on the electrocodeposition of matrix metal nanocomposites, Electrochim. Acta. 52 (2007) 7362–7371. https://doi.org/10.1016/j.electacta.2007.06.009.

[15] C. Li, M. Iqbal, J. Lin, X. Luo, B. Jiang, V. Malgras, K.C.W. Wu, J. Kim, Y. Yamauchi, Electrochemical Deposition: An Advanced Approach for Templated Synthesis of Nanoporous Metal Architectures, Acc. Chem. Res. 51 (2018) 1764–1773. https://doi.org/10.1021/acs.accounts.8b00119.

[16] R. Pollina, E. Valles, V. Gomez, Gómez et al (1994), J Electroanal Chem. 386 (1995) 45–56.

[17] M. Cortés, E. Gómez, E. Vallés, Electrochemical preparation and characterisation of CoPt magnetic particles, Electrochem. Commun. 12 (2010) 132–136. https://doi.org/10.1016/j.elecom.2009.11.006.

[18] E.A. Mernissi Cherigui, K. Sentosun, P. Bouckenooge, H. Vanrompay, S. Bals, H. Terryn, J. Ustarroz, Comprehensive Study of the Electrodeposition of Nickel Nanostructures from Deep Eutectic Solvents: Self-Limiting Growth by Electrolysis of Residual Water, J. Phys. Chem. C. 121 (2017) 9337–9347. https://doi.org/10.1021/acs.jpcc.7b01104.

[19] E. Gómez, J. Ramirez, E. Vallés, Electrodeposition of Co-Ni alloys, J. Appl. Electrochem. 28 (1998) 71–79. https://doi.org/10.1023/A:1003201919054.

[20] S.Z. El Abedin, M. Pölleth, S.A. Meiss, J. Janek, F. Endres, Ionic liquids as green electrolytes for the electrodeposition of nanomaterials, Green Chem. 9 (2007) 549–55. https://doi.org/10.1039/b614520e.

[21] K. Haerens, S. Van Deuren, E. Matthijs, B. Van der Bruggen, Challenges for recycling ionic liquids by using pressure driven membrane processes, Green Chem. 12 (2010) 2182–2188. https://doi.org/10.1039/c0gc00406e.

[22] M. Petkovic, K.R. Seddon, L.P.N. Rebelo, C.S. Pereira, Ionic liquids: A pathway to environmental acceptability, Chem. Soc. Rev. 40 (2011) 1383–1403. https://doi.org/10.1039/c004968a.

[23] L.I.N. Tomé, V. Baião, W. da Silva, C.M.A. Brett, Deep eutectic solvents for the production and application of new materials, Appl. Mater. Today. 10 (2018) 30–50. https://doi.org/10.1016/j.apmt.2017.11.005.

[24] D. V. Wagle, H. Zhao, G.A. Baker, Deep eutectic solvents: Sustainable media for nanoscale and functional materials, Acc. Chem. Res. 47 (2014) 2299–2308. https://doi.org/10.1021/ar5000488.

[25] P. Sebastián, E. Torralba, E. Vallés, A. Molina, E. Gómez, Advances in Copper Electrodeposition in Chloride Excess. A Theoretical and Experimental Approach, Electrochim. Acta. 164 (2015) 187–195. https://doi.org/10.1016/j.electacta.2015.02.206.

[26] P. Sebastián, E. Vallés, E. Gómez, First stages of silver electrodeposition in a deep eutectic solvent. Comparative behavior in aqueous medium, Electrochim. Acta. 112 (2013) 149–158. https://doi.org/10.1016/J.ELECTACTA.2013.08.144.

[27] Y.H. You, C.D. Gu, X.L. Wang, J.P. Tu, Electrodeposition of Ni-Co alloys from a deep eutectic solvent, Surf. Coatings Technol. 206 (2012) 3632–3638. https://doi.org/10.1016/j.surfcoat.2012.03.001.

[28] A.P. Abbott, D. Boothby, G. Capper, D.L. Davies, R.K. Rasheed, Deep Eutectic Solvents Formed between Choline Chloride and Carboxylic Acids: Versatile Alternatives to Ionic Liquids, J. Am. Chem. Soc. 126 (2004) 9142–9147. https://doi.org/10.1021/ja048266j.

[29] Q. Zhang, K. De Oliveira Vigier, S. Royer, F. Jérôme, Deep eutectic solvents: Syntheses, properties and applications, Chem. Soc. Rev. 41 (2012) 7108–7146. https://doi.org/10.1039/c2cs35178a.

[30] P. Sebastián, V. Climent, J.M. Feliu, E. Gómez, Ionic Liquids in the Field of Metal Electrodeposition, in: Encycl. Interfacial Chem., 2018: pp. 690–700. https://doi.org/10.1016/b978-0-12-409547-2.13379-7.

[31] C. Ma, A. Laaksonen, C. Liu, X. Lu, X. Ji, The peculiar effect of water on ionic liquids and deep eutectic solvents, Chem. Soc. Rev. 47 (2018) 8685–8720. https://doi.org/10.1039/c8cs00325d.

[32] P. Sebastian, M.I. Giannotti, E. Gómez, J.M. Feliu, Surface Sensitive Nickel

Electrodeposition in Deep Eutectic Solvent, ACS Appl. Energy Mater. 1 (2018) 1016–1028. https://doi.org/10.1021/acsaem.7b00177.

[33] E. Gómez, E. Vallés, Platinum electrodeposition in an ionic liquid analogue. solvent stability monitoring, Int. J. Electrochem. Sci. 8 (2013) 1443–1458.

[34] A. Serrà, E. Gómez, I. V. Golosovsky, J. Nogués, E. Vallés, Effective ionic-liquid microemulsion based electrodeposition of mesoporous Co-Pt films for methanol oxidation catalysis in alkaline media, J. Mater. Chem. A. 4 (2016) 7805–7814. https://doi.org/10.1039/c6ta02035f.

[35] A. Serrà, E. Gómez, J.F. López-Barbera, J. Nogués, E. Vallés, Green electrochemical template synthesis of CoPt nanoparticles with tunable size, composition, and magnetism from microemulsions using an ionic liquid (bmimPF6), ACS Nano. 8 (2014) 4630–4639. https://doi.org/10.1021/nn500367q.

[36] J. García-Torres, E. Gómez, E. Vallés, Modulation of magnetic and structural properties of cobalt thin films by means of electrodeposition, J. Appl. Electrochem. 39 (2009) 233–240. https://doi.org/10.1007/s10800-008-9661-9.

[37] E. Gómez, E. Vallés, Thick cobalt coatings obtained by electrodeposition, J. Appl. Electrochem. 32 (2002) 693–700. https://doi.org/10.1023/A:1020194532136.

[38] M. Li, Z. Wang, R.G. Reddy, Cobalt electrodeposition using urea and choline chloride, Electrochim. Acta. 123 (2014) 325–331. https://doi.org/10.1016/j.electacta.2014.01.052.

[39] T. Le Manh, E.M. Arce-Estrada, I. Mejía-Caballero, J. Aldana-González, M. Romero-Romo, M. Palomar-Pardavé, Electrochemical Synthesis of Cobalt with Different Crystal Structures from a Deep Eutectic Solvent, J. Electrochem. Soc. 165 (2018) D285–D290. https://doi.org/10.1149/2.0941807jes.

[40] A.M.P. Sakita, R. Della Noce, C.S. Fugivara, A. V. Benedetti, On the cobalt and cobalt oxide electrodeposition from a glyceline deep eutectic solvent, Phys. Chem. Chem. Phys. 18 (2016) 25048–25057. https://doi.org/10.1039/c6cp04068c.

[41] E. Gómez, P. Cojocaru, L. Magagnin, E. Valles, Electrodeposition of Co, Sm and SmCo from a Deep Eutectic Solvent, J. Electroanal. Chem. 658 (2011) 18–24. https://doi.org/10.1016/j.jelechem.2011.04.015.

[42] C. Du, B. Zhao, X.-B. Chen, N. Birbilis, H. Yang, Effect of water presence on choline chloride-2urea ionic liquid and coating platings from the hydrated ionic liquid, Sci. Rep. 6 (2016) 29225.

[43] J. Clavilier, R. Faure, G. Guinet, R. Durand, Preparation of Monocrystalline Pt Microelectrodes and Electrochemical Study of the Plane Surfaces Cut in the Direction of the (111) and (110) Planes, J.Electroanal.Chem. 107 (1980) 205–209. https://doi.org/10.1016/S0022-0728(79)80022-4.

[44] P. Sebastián, E. Gómez, V. Climent, J.M. Feliu, Copper underpotential deposition at gold surfaces in contact with a deep eutectic solvent: New insights, Electrochem. Commun. 78 (2017) 51–55.

[45] M. Lukaczynska, E.A. Mernissi Cherigui, A. Ceglia, K. Van Den Bergh, J. De Strycker, H. Terryn, J. Ustarroz, Influence of water content and applied potential on the electrodeposition of Ni coatings from deep eutectic solvents, Electrochim. Acta. 319 (2019) 690–704. https://doi.org/https://doi.org/10.1016/j.electacta.2019.06.161.

[46] P. Sebastian, M. Tułodziecki, M.P. Bernicola, V. Climent, E. Gómez, Y. Shao-Horn, J.M. Feliu, Use of CO as a Cleaning Tool of Highly Active Surfaces in Contact with Ionic Liquids: Ni Deposition on Pt(111) Surfaces in IL, ACS Appl. Energy Mater. 1 (2018) 4617–4625. https://doi.org/10.1021/acsaem.8b00776.

[47] G. Panzeri, J. Electrochem, D. Soc, G. Panzeri, L. Pedrazzetti, C. Rinaldi, L. Nobili, L. Magagnin, Electrodeposition of Nanostructured Cobalt Films from Choline Chloride- Ethylene Glycol Deep Eutectic Solvent Electrodeposition of Nanostructured Cobalt Films from Choline Chloride-Ethylene Glycol Deep Eutectic Solvent, J. Electrochem. Soc. 165 (2018) 8–12. https://doi.org/10.1149/2.0031813jes.

[48] G. Panzeri, A. Accogli, E. Gibertini, S. Varotto, C. Rinaldi, L. Nobili, L. Magagnin, Electrodeposition of cobalt thin films and nanowires from ethylene glycol-based solution, Electrochem. Commun. 103 (2019) 31–36.

https://doi.org/https://doi.org/10.1016/j.elecom.2019.04.012.

[49] N.M. Pereira, O. Brincoveanu, A.G. Pantazi, C.M. Pereira, J.P. Araújo, A. Fernando Silva, M. Enachescu, L. Anicai, Electrodeposition of Co and Co composites with carbon nanotubes using choline chloride-based ionic liquids, Surf. Coatings Technol. 324 (2017) 451–462. https://doi.org/https://doi.org/10.1016/j.surfcoat.2017.06.002.

[50] M.R. Ehrenburg, E.B. Molodkina, P. Broekmann, A. V. Rudnev, Underpotential Deposition of Silver on Au(111) from an Air- and Water-Stable Ionic Liquid Visualized by In-Situ STM, ChemElectroChem. (2018) 1–9. https://doi.org/10.1002/celc.201801404.

[51] E. Herrero, L.J. Buller, H.D. Abruña, Underpotential Deposition at Single Crystal Surfaces of Au, Pt, Ag and Other Materials, Chem. Rev. 101 (2001) 1897–1930. https://doi.org/10.1021/cr9600363.

[52] Q. Rayée, T. Doneux, C. Buess-Herman, Underpotential deposition of silver on gold from deep eutectic electrolytes, Electrochim. Acta. 237 (2017) 127–132. https://doi.org/https://doi.org/10.1016/j.electacta.2017.03.182.

[53] C. Giannini, M. Ladisa, D. Altamura, D. Siliqi, T. Sibillano, L. De Caro, X-ray Diffraction: A powerful technique for the multiple-length-scale structural analysis of nanomaterials, Crystals. 6 (2016) 1–22. https://doi.org/10.3390/cryst6080087.

[54] F. Ma, Y. Qin, Y.Z. Li, Enhanced microwave performance of cobalt nanoflakes with strong shape anisotropy, Appl. Phys. Lett. 96 (2010). https://doi.org/10.1063/1.3432441.

[55] M.C. Biesinger, L.W.M. Lau, A.R. Gerson, R.S.C. Smart, Resolving surface chemical states in XPS analysis of first row transition metals, oxides and hydroxides: Sc, Ti, V, Cu and Zn, Appl. Surf. Sci. 257 (2010) 887–898. https://doi.org/10.1016/j.apsusc.2010.07.086.

[56] M. Jana, P. Sivakumar, M. Kota, M.G. Jung, H.S. Park, Phase- and interlayer spacing-controlled cobalt hydroxides for high performance asymmetric supercapacitor applications, J. Power Sources. 422 (2019) 9–17. https://doi.org/10.1016/j.jpowsour.2019.03.019.

[57] P.F. Liu, S. Yang, L.R. Zheng, B. Zhang, H.G. Yang, Electrochemical etching of α-cobalt hydroxide for improvement of oxygen evolution reaction, J. Mater. Chem. A. 4 (2016) 9578–9584. https://doi.org/10.1039/c6ta04078k.

[58] T. Xue, X. Wang, J.M. Lee, Dual-template synthesis of Co(OH) 2 with mesoporous nanowire structure and its application in supercapacitor, J. Power Sources. 201 (2012) 382–386. https://doi.org/10.1016/j.jpowsour.2011.10.138.

[59] J.K. Chang, C.M. Wu, I.W. Sun, Nano-architectured Co(OH)2 electrodes constructed using an easily-manipulated electrochemical protocol for high-performance energy storage applications, J. Mater. Chem. 20 (2010) 3729–3735. https://doi.org/10.1039/b925176f.

Figure Captions:

Figure 1: Cyclic voltammograms recorded at 50 mV s^{-1} for the Co deposition on glassy carbon (GC) from DES + 0.1M $CoCl_2$ solution at 70 ºC (A, B) at different cathodic potential limits of (A, curve a) -1.23 V, (A, curve b) -1.36 V, (B, curve a) -1.55 V, and (B, curve b) -1.68 V. Curves (c) in Figure 1A and 1B corresponded to the blank solution. (C, D) Cyclic voltammograms recorded at a continuous scan (C and D, curves a) and after holding the potential at E = -1.2 V for 30 s (C, curve b) and E = -1.39 V for 60 s (D, curve b).

Figure 2: (A) j-t transients and (B) E-t transients for the Co deposition on glassy carbon electrodes recorded in DES + 0.1M $CoCl_2$ solution at 70 ºC.

Figure 3: FE-SEM micrographs of Co deposits prepared on glassy carbon electrodes using a DES + 0.1M $CoCl_2$ solution at 70 ºC and at (A) E = -1.10 V, (B) E = -1.15 V, and (C) E = -1.30 V.

Figure 4: (A, B) Cyclic voltammograms recorded at 50 mV s^{-1} for the Co deposition on a platinum polycrystalline bead from DES + 0.1M $CoCl_2$ solution at 70 ºC and at different potential limits of (A, curve a) -0.95 V, (A, curve b) -1.00 V, (B, curve a) -1.31 V, and (B, curve c) -1.63 V. Curves (c) in Figure 4A and (b) in Figure 4B corresponded to the blank solution. (C) j-t transients and (D) E-t transients of Pt recorded in DES + 0.1M $CoCl_2$ solution at 70 ºC.

Figure 5: FE-SEM micrographs of Co deposits prepared on Pt ball electrodes using a DES + 0.1M $CoCl_2$ solution at 70 ºC and at (A) E = -0.94 V, and (B) E = -0.99 V.

Figure 6: AFM contact-mode height (left) and deflection (right) images of Pt(111) modified by cobalt obtained by applying: A) -0.50 V during 10 s, B) -0.65 V during 3 s and C) -0.68 V during 10 s.

Figure 7: (A) Cyclic voltammograms recorded at 50 mV s^{-1} for the Co deposition on a gold polycrystalline bead from DES + 0.1M $CoCl_2$ solution at 70 ºC at different potential limits: (a) -1.15 V, (b) -1.3 V, (c) -1.5 V. Curve (d) corresponded to the blank solution. The inset shows the nucleation loop (red curve) and the previous Co UPD deposition magnified by a factor of 10. (B, C) FE-SEM micrographs of Co deposits prepared on Au electrodes using a DES + 0.1M $CoCl_2$ solution at 70 ºC and at (A) E = -0.93 V, and (B) E = -0.98 V.

Figure 8: XRD patterns both (non –magnified (left) and magnified (right)) of the Si/Ti/Au substrates (curves i) and prepared Co deposits on Si/Ti/Au substrates at E = -0.96 V (curves ii) and E = -1.35 V (curves iii).

Figure 9: XPS Co 2p and O 1s as a function of the sputter cycle for the prepared deposits at (A) E = -0.9 V and (B) E = -1.35 V. The deconvoluted curves correspond to the XPS spectrum after 40 sputter cycles.

Table 1: Q_{ox}/Q_{red} ratio calculated from the integration of the CVs of Co voltammetric curves on GC at different negative potential limits. v = 50 mV s^{-1}.

Electrode	**Negative limit**	**Q_{ox}/ Q_{red}**
GC	1.23V	0.96
GC	1.36V	0.76
GC	1.55V	0.39
GC	1.68V	0.20

Table 1

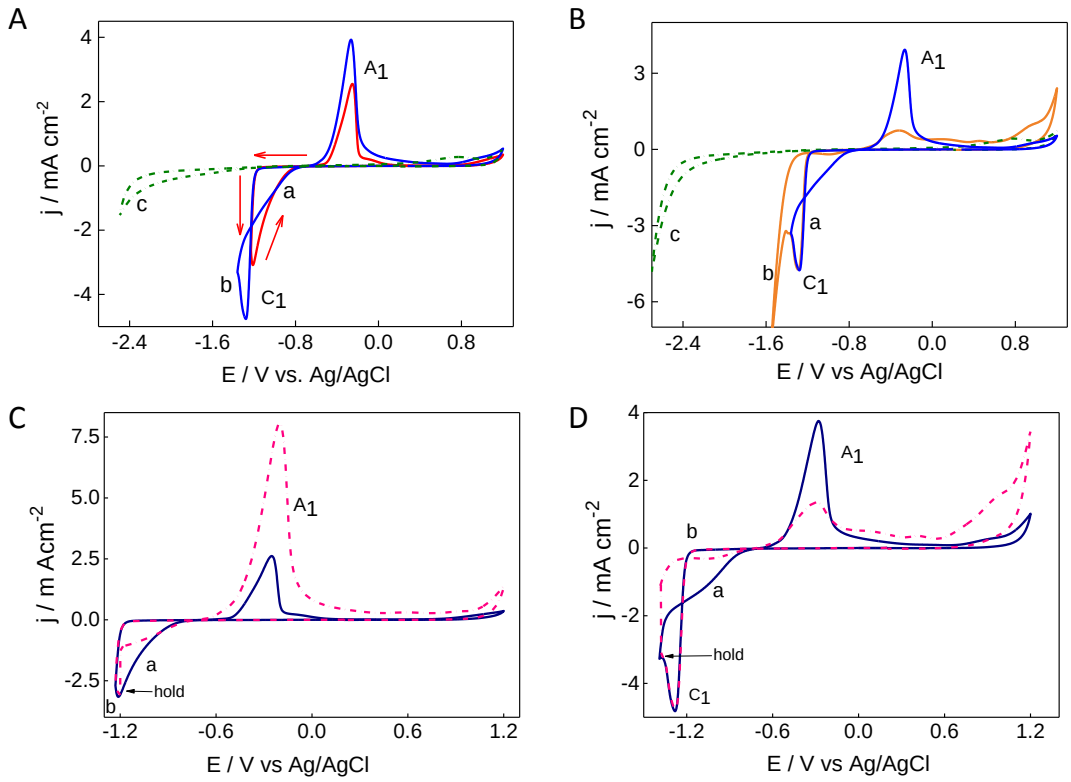

Figure 1

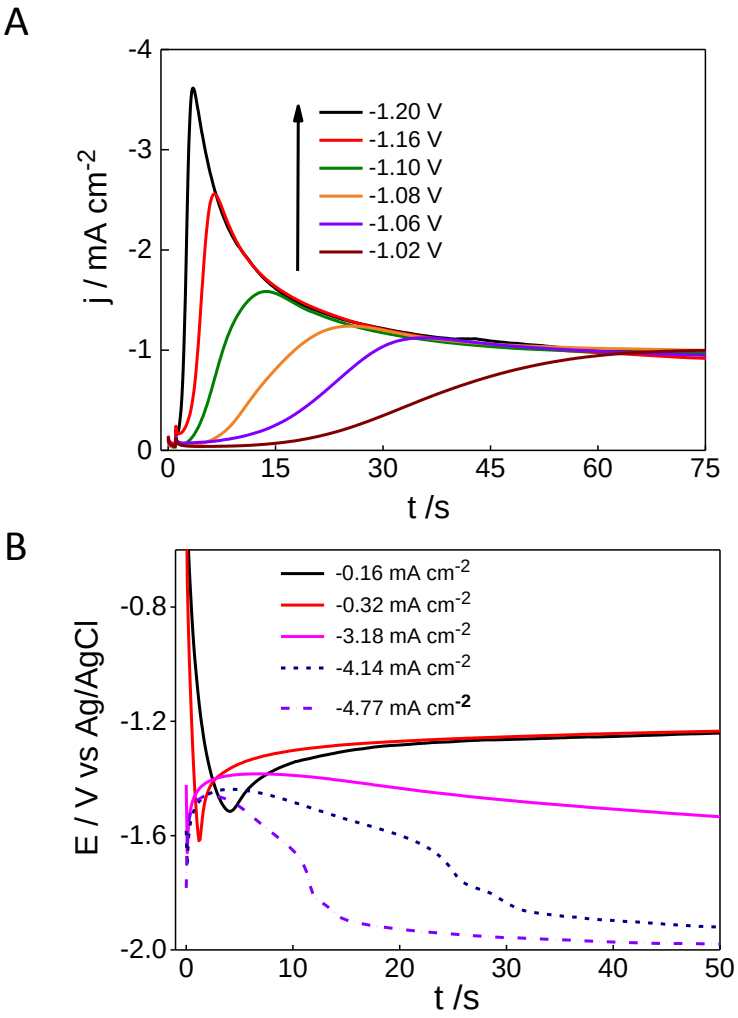
A
-4
-3
-2
-1
0
j / mA cm-2
-1.20 V
-1.16 V
-1.10 V
-1.08 V
-1.06 V
-1.02 V
0
15
30
45
60
75
t /s
B
-0.16 mA cm-2
-0.32 mA cm-2
-3.18 mA cm-2
-4.14 mA cm-2
-4.77 mA cm-2
-0.8
-1.2
-1.6
-2.0
E / V vs Ag/AgCl
0
10
20
30
40
50
t /s

Figure 2

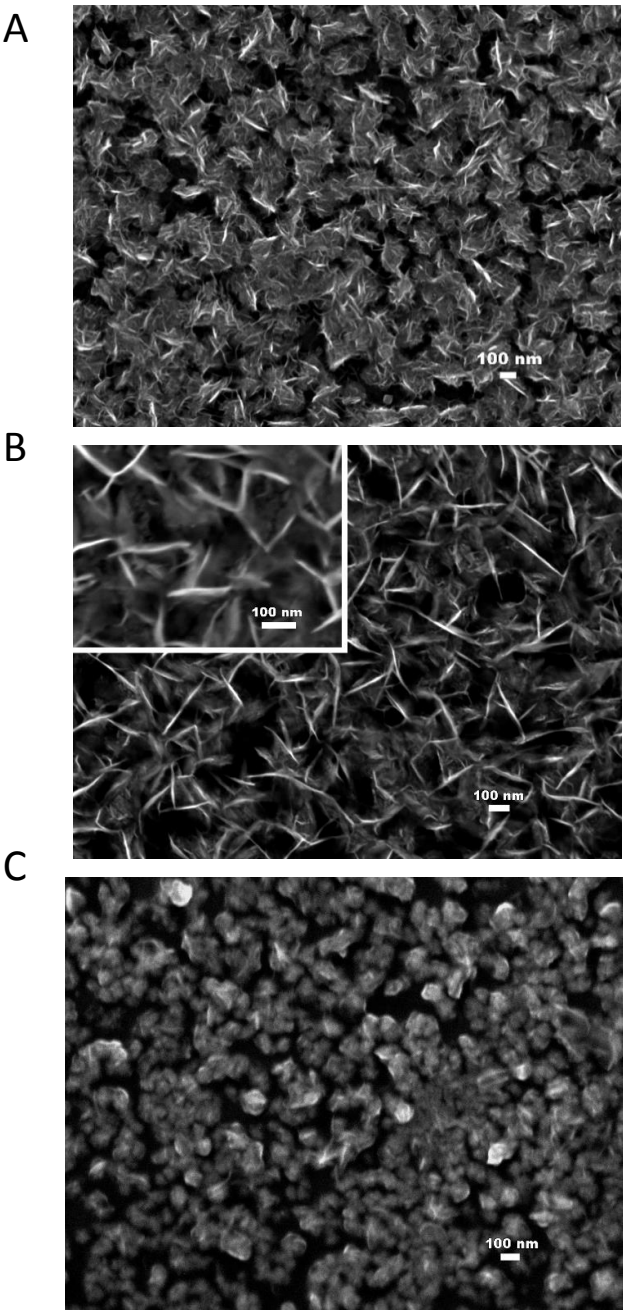

Figure 3

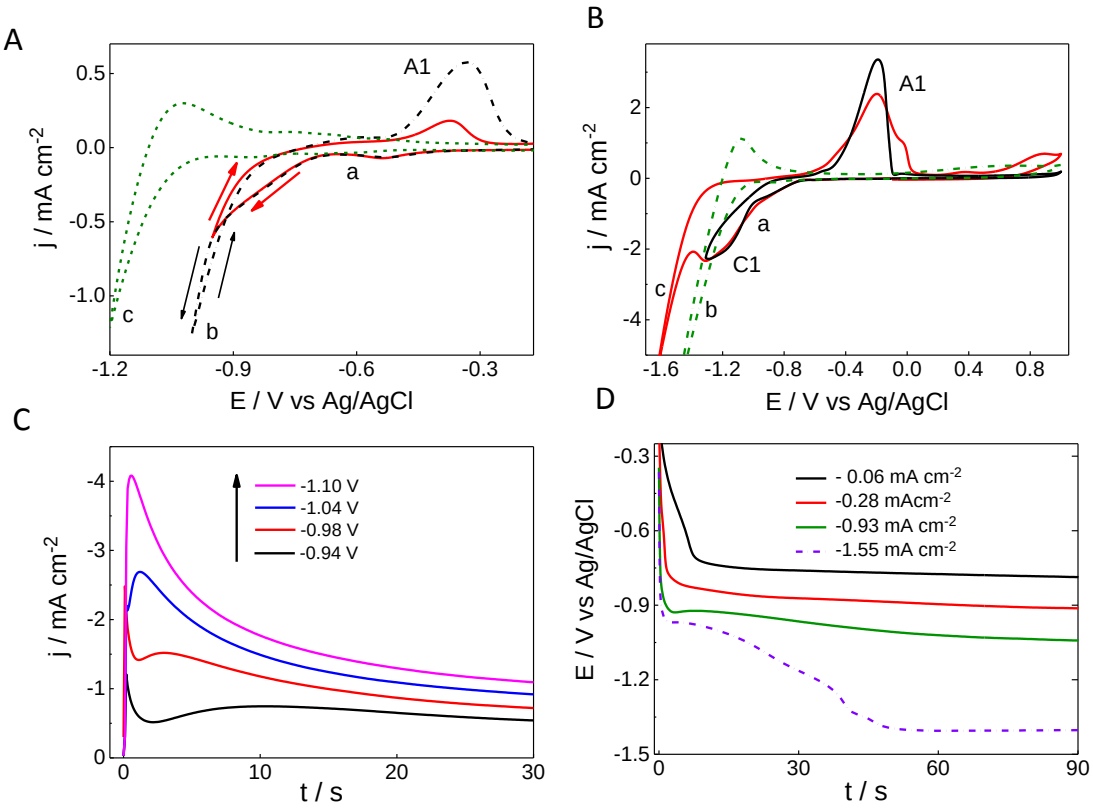
A
B
C
D
A1
a
b
c
C1
j / mA cm-2
E / V vs Ag/AgCl
t / s
-1.10 V
-1.04 V
-0.98 V
-0.94 V
- 0.06 mA cm-2
-0.28 mAcm-2
-0.93 mA cm-2
-1.55 mA cm-2

Figure 4

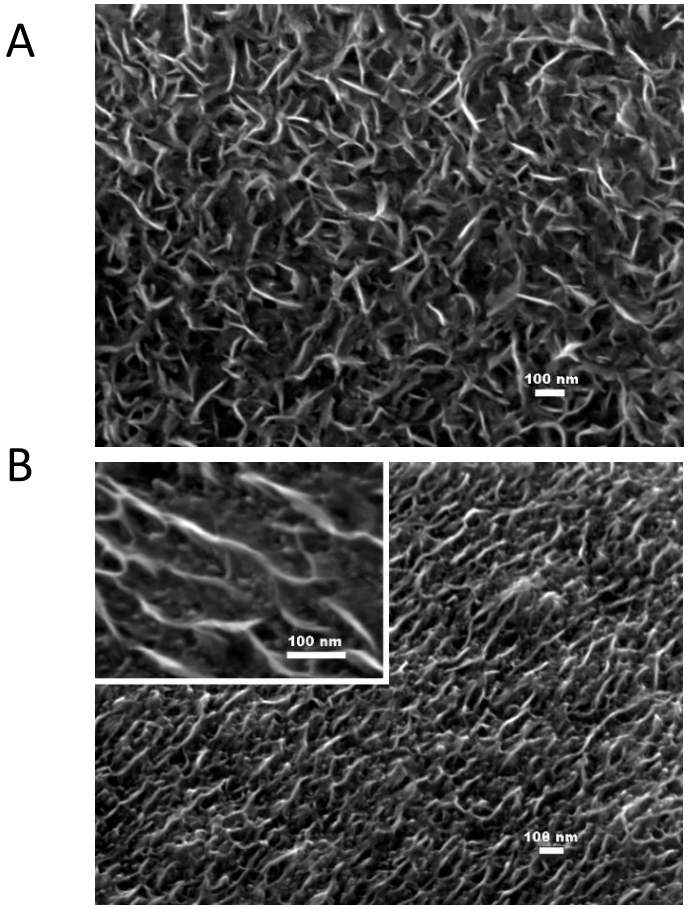

Figure 5

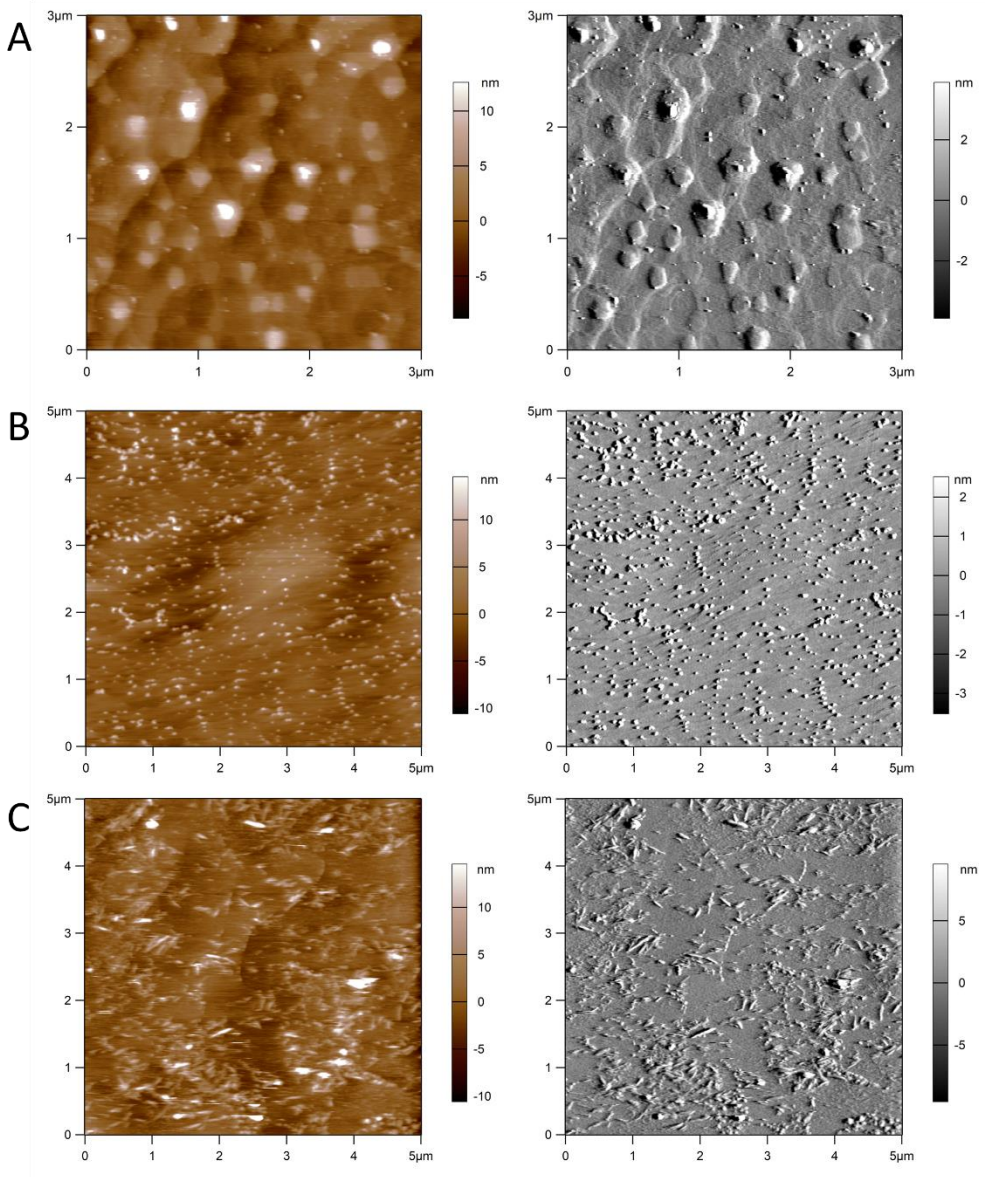

Figure 6

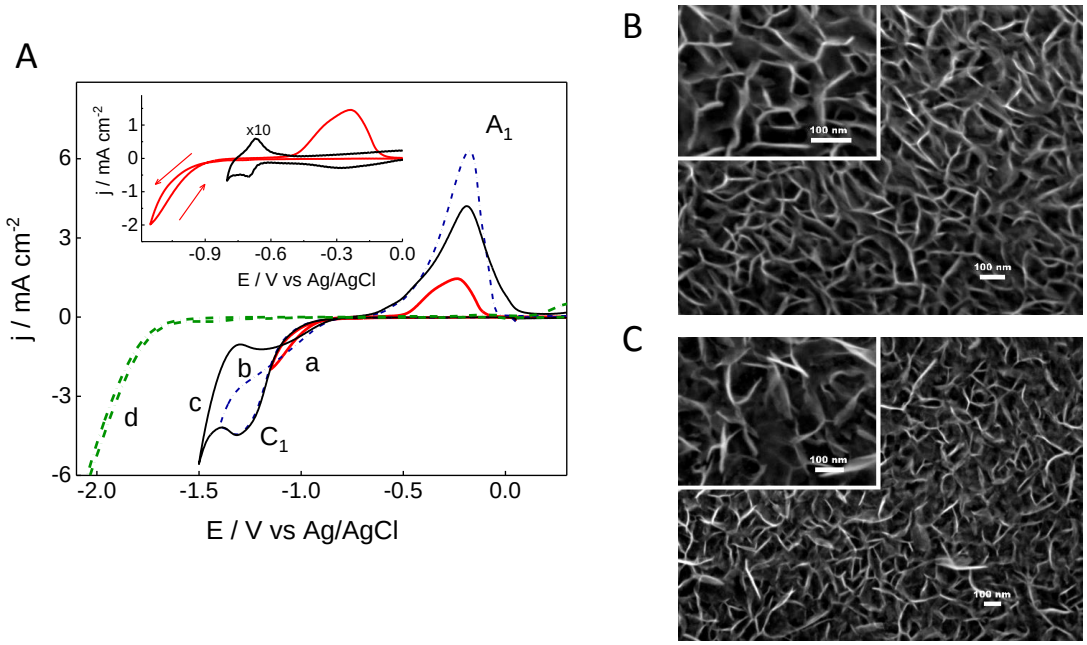

Figure 7

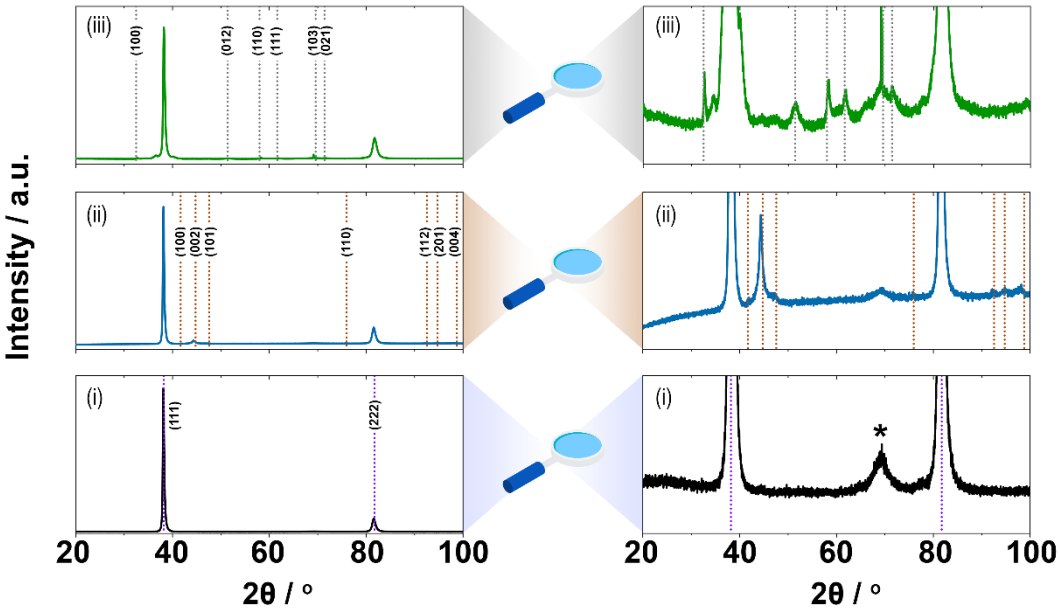
(iii)
(100)
(012)
(110)
(111)
(103)
(021)
(ii)
(100)
(002)
(101)
(110)
(112)
(201)
(004)
(i)
(111)
(222)
*
Intensity / a.u.
20
40
60
80
100
2θ / °

Figure 8

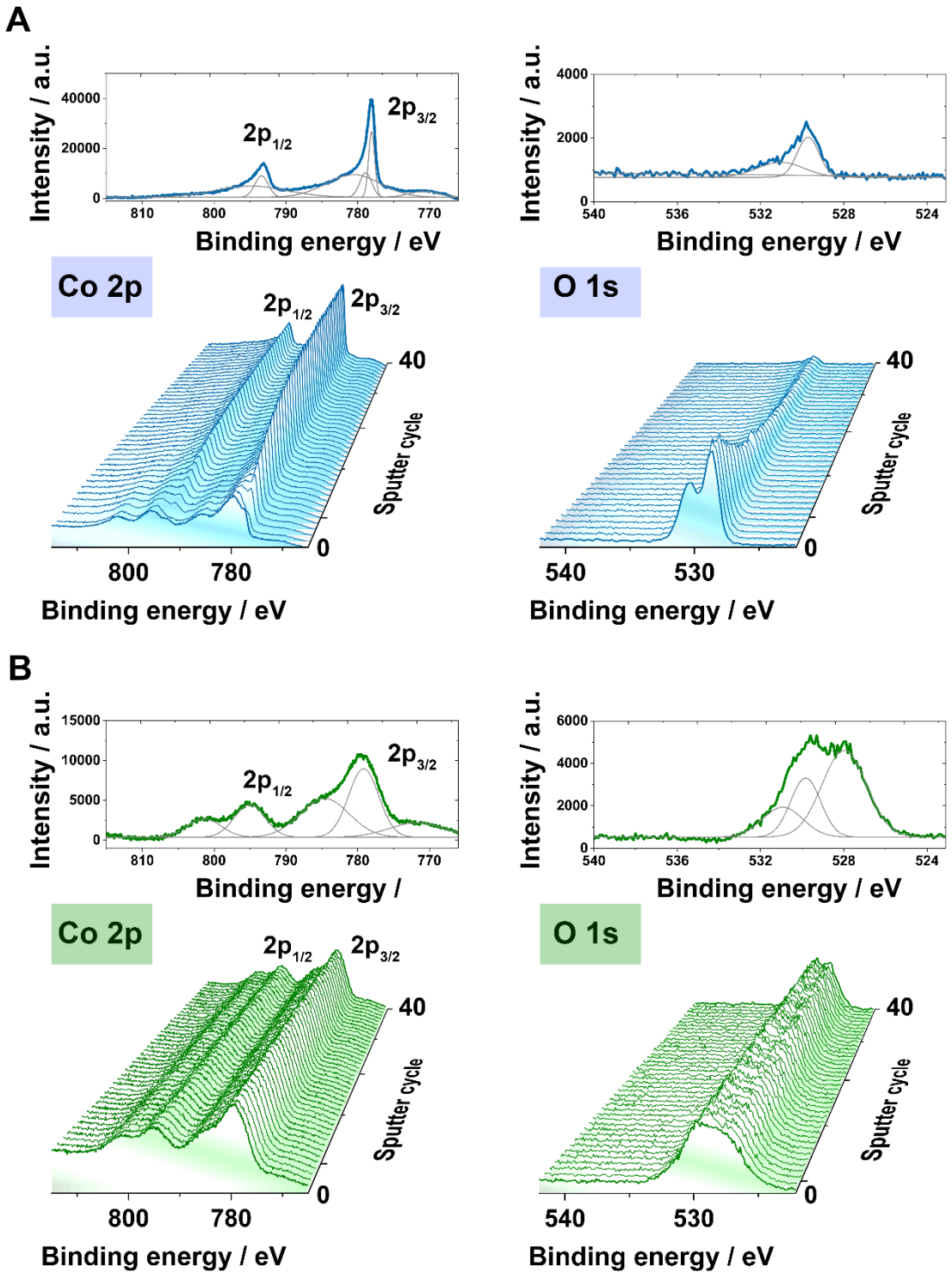
A
Intensity / a.u.
40000
20000
0
2p1/2
2p3/2
810
800
790
780
770
Binding energy / eV
Co 2p
2p1/2
2p3/2
40
Sputter cycle
0
800
780
Binding energy / eV
Intensity / a.u.
4000
2000
0
540
536
532
528
524
Binding energy / eV
O 1s
40
Sputter cycle
0
540
530
Binding energy / eV
B
Intensity / a.u.
15000
10000
5000
0
2p1/2
2p3/2
810
800
790
780
770
Binding energy /
Co 2p
2p1/2
2p3/2
40
Sputter cycle
0
800
780
Binding energy / eV
Intensity / a.u.
6000
4000
2000
0
540
536
532
528
524
Binding energy / eV
O 1s
40
Sputter cycle
0
540
530
Binding energy / eV

Figure 9